Dynamic Frictional Constraints in Translation and Rotation

Stuart A. Bowyer and Ferdinando Rodriguez y Baena

Abstract— **Active constraints and virtual fixtures are popular control strategies used within human-robot collaborative manipulation tasks, particularly in the field of robot-assisted surgery. Recent research has shown how active constraints, which robotically regulate the motion of a tool that is primarily manipulated by a human, can be implemented in dynamic environments which change and deform throughout a procedure. In a dynamic environment, movement of the constraint boundary can cause active forcing of the surgical tools, potentially reducing the surgeon's control and jeopardising patient safety. Dynamic frictional constraints have been proposed as a method for enforcing dynamic active constraints which do not generate energy of their own, and simply dissipate or redirect the energy of the surgeon to provide assistance. In this paper, dynamic frictional constraints are reformulated to allow formal proof that they are indeed dissipative, and hence also passive. This new formulation is then extended such that dynamic frictional constraints can simultaneously constrain the position and orientation of a tool. Experimental results show that the method is of significant benefit in performing a dynamic task when compared to cases without any assistance; with position and orientation constraints individually and with a conventional frictional constraint without energy redirection.**

I. INTRODUCTION

Active constraints [1] (also known as virtual fixtures [2]) are robot control strategies used to provide assistance in human-robot collaborative manipulation tasks [3]. Within the literature there are different variations on the concept, but in general, active constraints use a robot to anisotropically regulate the motion of a tool which is primarily manipulated, either directly or remotely, by a human user. The motion regulation imparted by the robot is typically used to either bound the tool to within a certain spatial region, or guide the tool in moving along a pathway.

The majority of active constraint research focuses specifically on methods for robot assisted surgery. Active constraints are well suited to this field because of the way in which they can combine the complementary proficiencies of humans and robots.

Much of the early active constraint research was applied in rigid environments, where the constraint geometries could be considered to be static throughout a procedure. Recently, however, several research groups have investigated the application of active constraints to soft tissue environments which deform or move over time, so called *dynamic* active constraints [4], [5].

In a previous publication by the authors of this paper, the energetic interaction between a user and a dynamic active constraint was investigated [6]. It was shown that implementing a conventional elastic constraint in a dynamic environment can lead to energetic activity in a robot, which could in turn cause active forcing of the surgical tools, reducing the surgeon's overall control of the procedure. This transfer in motive control from the surgeon to the robot can have implications for patient safety and clinical certification, therefore a new constraint formulation was proposed.

In [6], a constraint based on friction was selected as the solution to the problem of energy generation. Previously, Kikuuwe *et al*. created the non-energy storing *simulated plasticity* method of implementing constraints in static environments [7]. Simulated plasticity uses an anisotropic proxy model to compute a large (plastic) friction force when moving into a constrained region and a low (plastic) force when moving out. The challenge with implementing friction models, such as simulated plasticity, is that, once the user has penetrated the constraint, they could continue to remain within the constraint, moving parallel to the surface, indefinitely. *Frictional redirection* was the novel method proposed in [6] to overcome this. The method operated by applying the friction model non-orthogonally to the surface so that some component of the user's parallel motion would generate a force which guided them back to the surface, while continuing to remain dissipative.

In this paper, two developments to the dynamic frictional constraint formulation from [6] are made. Firstly, the model is reformulated in Euclidean space $\mathbb{R}^3$ in such a way that it can be proven to be dissipative. Secondly, it is shown how rotations in the 3-D special orthogonal group SO(3) can be mapped into Euclidean space such that six degree of freedom (DOF) dynamic frictional constraints can be applied simultaneously in position and orientation.

In section II the reformulation of dynamic frictional constraints in $\mathbb{R}^3$ and their extension to SO(3) is explained. Section III details the experimental method used to validate the efficacy of the proposed method, the results for which are given in section IV. A discussion of the results is given in section V and conclusions are drawn in section VI.

II. 6-DOF DYNAMIC FRICTIONAL CONSTRAINTS

In [6], 3-D constraints were achieved by rotating a modified version of the 1-D elasto-plastic (EP) friction model [8] in 3-D space. It operated so that when the user attempted to move into a constrained region, they were opposed by the friction force and when they retracted from the constraint they were not.

The primary novelty in the initial publication, which extended earlier work on friction based constraints by Kikuuwe

S. A. Bowyer and F. Rodriguez y Baena are with the Department of Mechanical Engineering, Imperial College London, London. SW7 2AZ. UK. f.rodriguez@imperial.ac.uk

et al. [7], was the conception of frictional redirection. It was noticed that, if a frictional constraint is applied which simply opposes penetration and permits retraction, then, once a user penetrates the constraint, they will never be pushed back out. The user will be able to move parallel to the surface, inside the constrained region, indefinitely. It could be argued that in a static constraint a high friction force will prevent any penetration; however, in a dynamic environment, the surface can move past the tool making constraint penetration likely.

Frictional redirection is illustrated in figures 3 and 5 of [6]. The method works by rotating the 1-D friction model as a function of the user's direction of motion. When the user moves directly into, or out, of the constraint, the friction model acts as stated above. Importantly, when the user moves approximately parallel to the constraint surface, the friction model is oriented at an angle so that some component of the friction force is towards the constraint surface, redirecting the user's motion to reduce the magnitude of the penetration.

The experiments in [6] showed the efficacy of the method in a dynamic path following task. For extension into SE(3) a reformulation of frictional redirection was employed which maintained the same energetic properties but permitted a unified consideration of translation and rotation. Details of this formulation are given in this section.

A. Elasto-plastic Friction Model in SE(3)

At the core of the dynamic frictional constraint concept was the discrete EP friction model conceived by Hayward *et al*. [8]. There are two primary reasons for the selection of the EP model. The first is that it is based on the well-established LuGre friction model [9] and the second is that it avoids issues with slow drift which would be unacceptable for a constraint.

The EP model is illustrated in figure 1. In this model, an object under friction has two components to its total displacement $x(t)$. The elastic displacement $z(t)$ defines a small amount of elastic pre-sliding and the plastic displacement $w(t)$ defines the position to which the object would return if all external forces were removed.

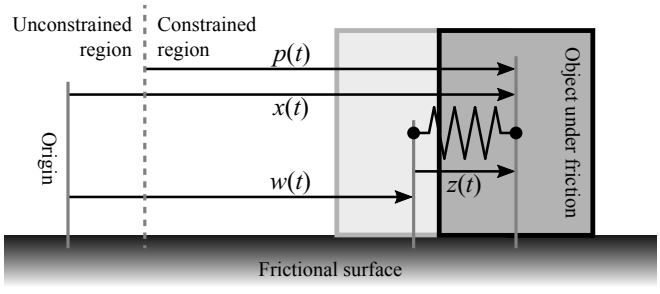


Fig. 1. Illustration of the vectorial EP model used within dynamic frictional constraints. An object's total displacement $x(t)$ is the sum of plastic $w(t)$ and elastic $z(t)$ components. In a dynamic frictional constraint, the variable $p(t)$ is included to identify the depth of constraint penetration.

In the EP model, $z(t)$ is an internal state variable which is updated, based on the object's total displacement $x(t)$, at each time-step. Using an elastic model of $z(t)$, the friction force f_f can then be computed using gains $\sigma_{0,1,2}$, as follows:

$$f_f(t) = \sigma_0 z(t) + \sigma_1 \dot{z}(t) + \sigma_2 \dot{x}(t) \tag{1}$$

In the EP model, the value of $z(t)$ is updated at each time-step using two saturation operations (equations (12) and (13) in [8]). The EP model was originally developed as a way to simulate physical frictional properties such as Stribeck curves; however, for application to constraints these are unnecessary. A simple Coulomb friction model, where the Coulomb force f_C is the maximum renderable constraint force, is sufficient. As proven in the appendix, in this case the full EP model at discrete time-step k reduces to:

$$z_k = \begin{cases} z_c & |z_c| < z_{css} \\ z_{css} & z_c \geq z_{css} \\ -z_{css} & z_c \leq -z_{css} \end{cases} \tag{2}$$

where z_c is the candidate z value and z_{css} is the Coulomb, steady state z value:

$$z_c = z_{k-1} + \Delta x_k \tag{3}$$

$$z_{css} = f_C/\sigma_0 \tag{4}$$

Intuitively, this shows that z_k is computed by first establishing what its value would be if the displacement was purely elastic z_c and then clamping this value to $\pm z_{css}$.

To extend the 1-D, discrete EP model into 6-D, each of the displacement components (i.e. $x(t)$, $w(t)$ and $z(t)$) must be represented in the special Euclidean group SE(3). In this work, the total displacement of an object from an inertial frame in SE(3) is defined as $\mathbf{x}(t) \in \mathbb{R}^6$. $\mathbf{x}(t)$ and its time derivative $\dot{\mathbf{x}}(t)$ are defined as follows:

$$\mathbf{x}(t) = [\mathbf{x}_t(t), \mathbf{x}_r(t)] \tag{5}$$

$$\dot{\mathbf{x}}(t) = [\dot{\mathbf{x}}_t(t), \dot{\mathbf{x}}_r(t)] \tag{6}$$

where $\mathbf{x}_t(t) \in \mathbb{R}^3$ is the translational displacement, $\mathbf{x}_r(t) \in \mathbb{R}^3$ is the rotational displacement in SO(3), represented as a rotation vector, $\dot{\mathbf{x}}_t(t) \in \mathbb{R}^3$ is the translational velocity and $\dot{\mathbf{x}}_r(t) \in \mathbb{R}^3$ is the angular velocity in SO(3). These $\mathbb{R}^6$ vectors are defined similarly for $\mathbf{w}(t)$, $\mathbf{z}(t)$ and $\mathbf{p}(t)$.

Using these vector representations for the three components of the frictional displacement, equation (1) becomes:

$$\mathbf{f}_f(t) = \Sigma_0 \mathbf{z}(t) + \Sigma_1 \dot{\mathbf{z}}(t) + \Sigma_2 \dot{\mathbf{x}}(t) \tag{7}$$

where $\mathbf{f}_f(t) \in \mathbb{R}^6$ is the frictional force-torque value, and the three gain matrices $\Sigma \in \mathbb{R}^{6\times 6}$ are defined as follows:

$$\Sigma_i = \mathrm{diag}(\sigma_{t,i}, \sigma_{t,i}, \sigma_{t,i}, \sigma_{r,i}, \sigma_{r,i}, \sigma_{r,i}) \tag{8}$$

where $i = 0, 1, 2$. In these matrices, the scalar coefficients $\sigma_{t,0}$ and $\sigma_{r,0}$ define the friction stiffness in translation and rotation respectively; the scalar coefficients $\sigma_{t,1}$ and $\sigma_{r,1}$ define the tangential compliance damping in translation and rotation respectively; and the scalar coefficients $\sigma_{t,2}$ and $\sigma_{r,2}$ define the viscous friction coefficients in translation and rotation respectively.

In the remainder of this section the extension of the SE(3) EP model to dynamic frictional constraints will be explained. Due to the disconnection between translations in $\mathbb{R}^3$ and

rotations in SO(3), these will be considered independently in this work. Constraints which couple motion in translation and rotation are left for future work.

B. Dynamic Frictional Constraints in $\mathbb{R}^3$

For translations in $\mathbb{R}^3$, the scalar clamping operation in equation (2) can be thought of as clamping a candidate $\mathbf{z}_{t,c}$ value to within a 3-D sphere, centred at the origin, with a radius $z_{t,css}$:

$$\mathbf{z}_{t,k} = \begin{cases} \mathbf{z}_{t,c} & \mathbf{z}_{t,c} < z_{t,css} \\ z_{t,css}\hat{\mathbf{z}}_{t,c} & otherwise \end{cases} \tag{9}$$

where:

$$\mathbf{z}_{t,c} = \mathbf{z}_{t,k-1} + \Delta\mathbf{x}_{t,k} \tag{10}$$

$$\hat{\mathbf{z}}_{t,c} = \mathbf{z}_{t,c}/\|\mathbf{z}_{t,c}\| \tag{11}$$

$$z_{t,css} = f_C/\sigma_{t,0} \tag{12}$$

Implementing the model in equation (9) would generate isotropic friction forces which oppose motion in all directions of $\mathbb{R}^3$. Anisotropy and frictional redirection can be included by projecting $\mathbf{z}_{t,c}$ into a closed conical set $C_t \subset \mathbb{R}^3$ rather than a spherical one. The conical subset of $\mathbb{R}^3$ is defined such that its axis is aligned with the constraint penetration vector $\mathbf{p}_{t,k}$, with an apex angle θ, as follows:

$$C_{t,k} = \left\{\mathbf{w} : \mathbf{w} \in \mathbb{R}^3, \Theta(\mathbf{w}, \mathbf{p}_{t,k}) \leq \theta, ||\mathbf{w}|| \leq z_{t,css}\right\} \tag{13}$$

where the binary function $\Theta(\cdot,\cdot)$ defines the angle between two vectors.

The computation of $\mathbf{z}_{t,k}$ for a dynamic frictional constraint in $\mathbb{R}^3$ is then given by the projection of $\mathbf{z}_{t,c}$ into $C_{t,k}$ as follows:

$$\mathbf{z}_{t,k} = \underset{\mathbf{w}\in C_{t,k}}{\arg\min}\|\mathbf{w} - \mathbf{z}_{t,c}\| \tag{14}$$

The closed-form expression of equation (14) for $C_{t,k}$ as defined in equation (13) is as follows:

$$\mathbf{z}_{t,k} = \begin{cases} \mathbf{z}_{t,c} & \Theta(\mathbf{z}_{t,c}, \mathbf{p}_{t,k}) \leq \theta \wedge \|\mathbf{z}_{t,c}\| \leq z_{t,css} \\ z_{t,css}\hat{\mathbf{z}}_{t,c} & \Theta(\mathbf{z}_{t,c}, \mathbf{p}_{t,k}) \leq \theta \wedge \|\mathbf{z}_{t,c}\| > z_{t,css} \\ \tilde{z}_{t,c}\hat{\mathbf{y}} & otherwise \end{cases} \tag{15}$$

where $\hat{\mathbf{y}}$ is a unit vector defining the edge of the cone $C_{t,k}$ on the plane through $\mathbf{z}_{t,c}$ and $\mathbf{p}_{t,k}$; and $\tilde{z}_{t,c}$ is the scalar projection of $\mathbf{z}_{t,c}$ onto $\hat{\mathbf{y}}$, clamped between 0 and $z_{t,css}$.

$$\tilde{z}_{t,c} = \begin{cases} 0 & \mathbf{z}_{t,c}\cdot\hat{\mathbf{y}} \leq 0 \\ \mathbf{z}_{t,c}\cdot\hat{\mathbf{y}} & 0 < \mathbf{z}_{t,c}\cdot\hat{\mathbf{y}} < z_{t,css} \\ z_{t,css} & otherwise \end{cases} \tag{16}$$

An illustration of the conical constraint formulation is given in figure 2. To understand its behaviour, the three constraint violation states used in [6] can be considered. When the user is orthogonally moving into the constraint (orthogonal violation) the angle between $\mathbf{z}_c$ and $\mathbf{p}$ is small and the projection operation will limit the magnitude of $\mathbf{z}_c$ to z_{css}. Here the model acts in the same way as the standard EP model in equation (9).

When the user is orthogonally retracting from the constraint (orthogonal retraction) the angle between $\mathbf{z}_c$ and $\mathbf{p}$ is almost $180°$ and the projection operation will set $\mathbf{z}_k$, and subsequently the friction force, to zero.

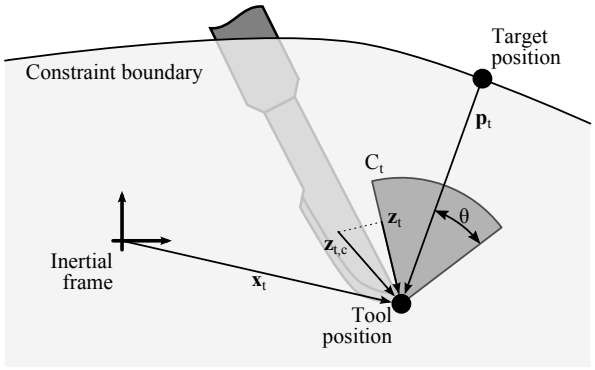


Fig. 2. Illustration of the proposed dynamic frictional constraints. Shown is an example of projecting the candidate $\mathbf{z}_{t,c}$ into the conical vector subset C_t to compute $\mathbf{z}_t$. The axis of the conical set is the constraint penetration vector $\mathbf{p}_t$ and it has an apex angle θ.

When the user is moving parallel to the surface of the constraint, but within it (parallel violation), $\mathbf{z}_c$ will be projected onto the edge of the cone. This projection means that some component of the friction force will be pushing the user towards the surface. It is in this case where the constraint exhibits frictional redirection such that the user is encouraged to retract from the constraint.

If θ is low, then the constraint will not exhibit much frictional redirection and will act largely like a conventional frictional constraint, such as in [7]. However, as θ increases, a larger and larger component of the motion parallel to the constraint will generate frictional redirection forces, reducing the constraint violation.

As this constraint formulation is based on a friction model, it dissipates the majority of the energy that is put in. Formal proof of the dissipativity of dynamic frictional constraints is shown in the appendix. It is known that a dissipative system is also passive [10], therefore it can be deduced that dynamic frictional constraints are also passive (subject to the inherent limitations of a discrete time system).

C. Dynamic Frictional Constraints in SO(3)

When applying dynamic frictional constraints to SO(3), the choice of rotation formalism requires consideration. Firstly, it must be possible to project a rotation into a finite, conical subset of the rotation space with a defined apex angle and radius. Secondly, when projecting into the conical subset, it must minimise the rotation angle between the candidate and projected orientations.

Initially, unit quaternions [11] were selected for use in applying dynamic frictional constraints in SO(3). Quaternion rotations have the unique property that the angle between any two vector representations (i.e. $\arccos(\mathbf{q}_1 \cdot \mathbf{q}_2)$) is exactly half the minimum angle between the two rotations that they represent. Moreover, the set of unit quaternions can be considered as a unit 3-sphere, $S^3 \subset \mathbb{R}^4$ and therefore the geodesic distance between any two quaternions on S^3 is also exactly half the minimum angle between the two rotations

that they represent. Subsequently, the direction of a geodesic between two quaternions gives the most direct rotation between them. It is this property that makes quaternions adept at interpolating between rotations using the spherical linear interpolation (SLERP) method [11].

The importance of the relationship between geodesics on S^3 and minimum rotation angles is that quaternions can be used to accurately describe a finite conical subset and they guarantee that a projection minimises the true rotational angle. An illustration of how the conical vector subset would look on a quaternion sphere is shown in figure 3. Here, rotations $\mathbf{z}_q$, $\mathbf{z}_{q,c}$, $\mathbf{x}_q$ and $\mathbf{p}_q$ are the quaternion equivalents of the rotation vectors $\mathbf{z}_r$, $\mathbf{z}_{r,c}$, $\mathbf{x}_r$ and $\mathbf{p}_r$ respectively.

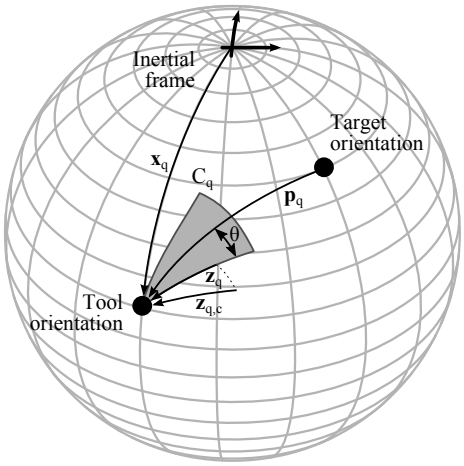


Fig. 3. Illustration of the conical projection method on the surface of a unit quaternion 3-sphere.

Ideally, it would be possible to apply the method from equation (15) directly to quaternion vectors in $\mathbb{R}^4$. However, these operations would not guarantee that the output remains as a valid unit quaternion in S^3. Instead, it is necessary to map the surface of the quaternion 3-sphere into $\mathbb{R}^3$ Euclidean space where the validity of the output is guaranteed.

In general, it is not possible to find a mapping from a manifold, such as S^3, into a Euclidean space where all relative distances and directions are preserved. However, for performing a conical projection, the azimuthal equidistant projection (AEP) [12] provides a suitable approximation. Fortunately, the result of applying AEP to a unit quaternion on S^3 is known, and the mapping is in fact equivalent to the conversion of quaternions into rotation vectors [13].

The AEP can be visualised as flattening out S^3, starting from the projection point, where both distances and azimuth angles of all points with respect to the projection point are preserved. By taking the AEP at the apex of the cone (i.e. $\mathbf{x}_q$), the preservation of distances means that the radius of the cone will be correct, and the preservation of azimuth angles means that the apex angle of the cone will also be correct. The problem with AEP is that the distance between point pairs which do not include the projection point are not preserved. This means that minimising the distance between $\mathbf{z}_{r,k}$ and $\mathbf{z}_{r,c}$ does not necessarily minimise the geodesic distance between $\mathbf{z}_{q,k}$ and $\mathbf{z}_{q,c}$ on S^3. However, as the radius of the cone is small, both $\mathbf{z}_{r,k}$ and $\mathbf{z}_{r,c}$ will be close to the origin, where the projection is almost Euclidean making, this difference negligible (as the results in section IV show).

To apply frictional redirection to rotational motion using the conical projection method, the constraint penetration vector $\mathbf{p}_{r,k}$ and the candidate z vector $\mathbf{z}_{r,c}$ must both be represented as rotation vectors. As combining rotation vectors is inefficient, the candidate $\mathbf{z}_{t,c}$ should first be computed as a quaternion, before converting into a rotation vector, as follows (taking consideration of the reference frame for each rotation):

$$\mathbf{z}_{q,c} = \Delta\mathbf{x}_{q,k} * \mathbf{z}_{q,k-1} \tag{17}$$

where $*$ is the quaternion product operation and $\Delta\mathbf{x}_{q,k}$ is the change in x orientation, with respect to the inertial frame:

$$\Delta\mathbf{x}_{q,k} = \mathbf{x}_{q,k} * \mathbf{x}_{q,k-1}^{-1} \tag{18}$$

Frictional redirection for rotation can be applied (similarly to equation (14)) by projecting the candidate rotation vector into the conical subset, as shown below. The actual implementation of this projection is the direct parallel of that for translation in equation (15) and is not reproduced here.

$$\mathbf{z}_{r,k} = \underset{\mathbf{w}\in C_{r,k}}{\arg\min} \|\mathbf{w} - \mathbf{z}_{r,c}\| \tag{19}$$

where the conical subset is given as:

$$C_{r,k} = \left\{\mathbf{w} : \mathbf{w} \in \mathbb{R}^3, \Theta(\mathbf{w}, \mathbf{p}_{r,k}) \leq \theta, ||\mathbf{w}|| \leq z_{r,css}\right\} \tag{20}$$

and where the cone's radius is computed from the Coulomb torque τ_C and rotational stiffness as follows:

$$z_{r,css} = \tau_C / \sigma_{r,0} \tag{21}$$

It can be shown that this projection operation in rotation is also dissipative by following the proof for translation in the appendix and assuming that the magnitude of $\mathbf{z}_{r,k}$ is small.

III. EXPERIMENTAL VALIDATION

A. Experimental Apparatus

The effectiveness of the proposed dynamic frictional constraint formulation was quantified with a simulated version of *The Steady-hand Game*. In this game, a user moves a ring along a curving wire pathway, while attempting to avoid the ring and wire making contact. This game is a test of both manual dexterity and hand-eye coordination for the user. The primary reason for selecting this game to validate dynamic frictional constraints is that the user must simultaneously control both the position and orientation of the ring.

The visualisation for the simulation was created using The Visualisation Toolkit (VTK, Kitware Inc.) and is shown in figure 4. To assist the user in determining the depth of the ring and wire within the scene, it was displayed on a 3-D monitor using NVIDIA 3D Vision (NVIDIA Corp.).

A W5D haptic device (Entact Robotics Inc.) allowed the user to control the position of the ring within the simulation and rendered the constraint forces and torques back to them. As the W5D only has five actuated degrees of freedom, the

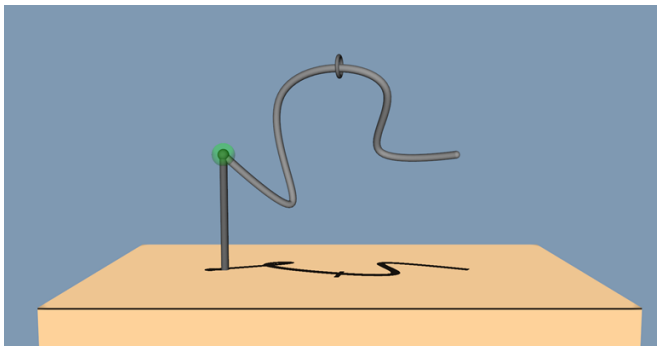


Fig. 4. Simulation of the steady-hand game used within the experiments. Shown is the user controlled ring, the deforming wire pathway and the active target towards which the user is moving.

non-actuated tool axis was aligned with the centre axis of the ring. As the ring is rotationally invariant around this axis, the lack of constraint torques had no effect on the task.

To validate the dynamic nature of the dynamic frictional constraints, the wire pathways within the simulated steady-hand game randomly deformed over time. The deformation was achieved by applying a bounded random walk to each control point of the cardinal spline that defined the wire pathway. For these experiments the speed of each deforming control point was set at approximately 20 mm.s^{-1}. The inner diameter of the ring was 14 mm and the diameter of the wire pathway was 8 mm.

The constraint control algorithms were implemented in C++ on a Linux PC with a 3 GHz Core 2 Duo CPU (Intel Corp.) at a haptic rate of 1 kHz. The 3-D visualisation was implemented in C++ on a Windows PC (Microsoft Corp.) with a 2.93 GHz Core i7-870 CPU (Intel Corp.)/Quadro 4000 GPU (NVIDIA Corp.) at a display rate of approximately 40 Hz. The user datagram protocol (UDP) was used to relay ring positions from the control PC to the visualisation PC.

B. Experimental Procedure

Five constraint methods were used to assist the test subjects within the experiments. These are shown below.

- **UC**- Unconstrained, no constraint forces or torques were applied.
- **DFC3T** - 3-D translational dynamic frictional constraints. As in section II-B, with no constraint torques.
- **DFC3R** - 3-D rotational dynamic frictional constraints. As in section II-C, with no constraint forces.
- **FC6** - 6-D frictional constraints without frictional redirection. Equivalent to DFC3T and DFC3R being applied simultaneously with $\theta = 0$ rad. This approximates a conventional static frictional constraint similar to that described in [7].
- **DFC6** - 6-D dynamic frictional constraints with frictional redirection in translation and rotation. Equivalent to DFC3T and DFC3R being applied simultaneously with $\theta = 0.4$ rad.

The constraints were applied based on an optimal target pose for the ring which maximised its separation from the wire. The target position was defined at the closest point on the centreline of the pathway to the ring's current position. The target orientation was defined as a coordinate frame at the target position where the axis of the ring was aligned with the tangent of the pathway. The closest points were found by exhaustively searching a discretised set of line segments which represented the centreline.

The parameters for the constraints were defined empirically based on the capabilities of the selected haptic device and are shown in table I.

TABLE I

PARAMETERS USED IN THE FRICTIONAL CONSTRAINTS.

Parameter	Value	Parameter	Value
f_C	3.0 N	τ_C	20 N.mm
$\sigma_{t,0}$	1.0 N.mm^{-1}	$\sigma_{r,0}$	100 N.mm.rad^{-1}
$\sigma_{t,1}$	0 N.s.mm^{-1}	$\sigma_{r,1}$	0 N.mm.s.rad^{-1}
$\sigma_{t,2}$	0.0025 N.s.mm^{-1}	$\sigma_{r,2}$	0.002 N.mm.s.rad^{-1}

Each subject was given a document explaining the experimental procedure and then they were allowed a period of time to familiarise themselves with the haptic device, simulation and task. After this training period, 36 test runs were undertaken. Six different wire pathways were used in the tests, each of which was run with all five of the constraint methods above. This gave a total of six runs, per subject, per constraint method. The ordering of the test runs was randomised and the users were not informed of the nature of the constraints, or which one was assisting them. The sole requirement placed upon the subject was that they avoid contact between the ring and the wire.

A total of 7 people took part in the experiments. This consisted of 6 (1) males (females), 5 (2) right (left) handed people and 2 (5) surgeons (non-surgeons), all of whom had previous experience with haptic simulations.

IV. RESULTS

Two primary metrics of the effectiveness of the constraint methods are presented. The first metric was the mean separation between the ring and pathway for each test run. The second metric was the percentage of the traversal for which the ring and pathway were in contact.

The means and standard deviations for each of these metrics, across all 42 test runs with each constraint method, is given in table II. The distributions within this table for ring-pathway separation and contact percentage are visualised in the box plots in figures 5 and 6 respectively.

One-way analysis of variance (ANOVA) tests were applied to the results from both ring-pathway separation and contact percentage; and in both cases they were found to be significantly affected by the constraint method used ($p < 10^{-6}$). Pairwise comparisons were subsequently made between each constraint method using Tukey's honest significant difference (HSD) test [14] at the 90 % and 95 % confidence intervals. The results from these pairwise comparisons are given for the ring-pathway separation and contact percentage in tables III and IV respectively. As expected, in all cases the mean

TABLE II

RESULTS FOR RING-PATHWAY SEPARATION AND CONTACT PERCENTAGES.

	Mean ring-pathway separation		Contact percentage	
	Mean	Stdev	Mean	Stdev
UC	0.14 mm	0.09 mm	82.2 %	9.5 %
DFC3T	1.20 mm	0.50 mm	23.4 %	22.4 %
DFC3R	0.17 mm	0.11 mm	82.1 %	10.8 %
FC6	1.06 mm	0.56 mm	34.0 %	23.9 %
DFC6	1.57 mm	0.50 mm	12.8 %	13.3 %

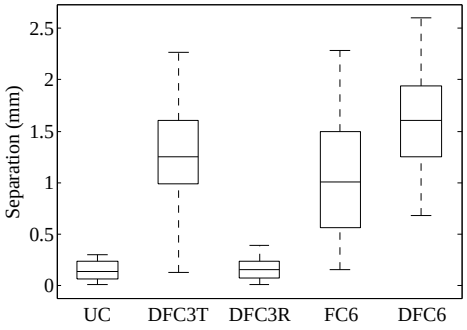


Fig. 5. Distributions of the mean separation between the ring and pathway.

power for each test was negative therefore these plots are not shown.

TABLE III

RESULTS OF THE TUKEY HSD TEST FOR RING-PATHWAY SEPARATION AT THE 95 % (**) AND 90 % (*) CONFIDENCE INTERVALS.

	DFC3T	DFC3R	FC6	DFC6
UC	**		**	**
DFC3T		**		**
DFC3R			**	**
FC6				**

TABLE IV

RESULTS OF THE TUKEY HSD TEST FOR CONTACT PERCENTAGE AT THE 95 % (**) AND 90 % (*) CONFIDENCE INTERVALS.

	DFC3T	DFC3R	FC6	DFC6
UC	**		**	**
DFC3T		**	*	*
DFC3R			**	**
FC6				**

V. DISCUSSION

The mean values for ring-pathway separation ranged between 0.14 mm and 1.57 mm. The mean contact percentages ranged between 12.8 % and 82.2 %. Higher mean separations and lower contact percentages identify constraint methods which were more effective at assisting the users.

The results show that, for both metrics, the lowest performance was unsurprisingly recorded during the unconstrained case (UC). The randomised deformation of the pathway meant that the task itself was difficult as it required quick reactions and high dexterity from the user. Without assistance, the majority of the test subjects were not physically able to successfully navigate along the pathway.

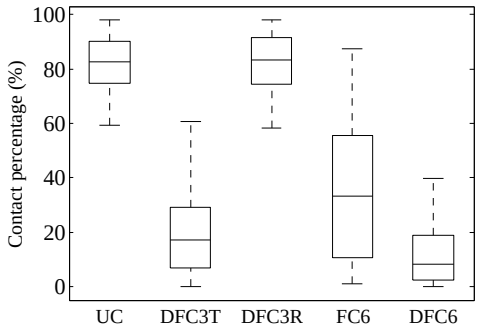


Fig. 6. Distributions of the contact percentage.

During the experiments where translational dynamic frictional constraints were applied (DFC3T), the average performance under both metrics significantly improved from UC. These results confirm those presented in [6] and, importantly, also show that constraining position is beneficial even when orientation is a factor in the task. The likely cause of this is that the cognitive load involved in positioning the ring is reduced to such a degree that the user has the time to actively consider and control the orientation as required for the task.

When dynamic frictional constraints were applied to rotation in isolation (DFC3R), the average performance under both metrics increased slightly from UC; however, this difference was not found to be statistically significant. During the tests of UC and DFC3R the users spent most of the time with the ring deeply embedded in, or completely pushed through, the pathway. The magnitude of the assistance that a rotational constraint can offer is much smaller than that for translation as at most it can only separate the ring and pathway by the inner radius of the ring. This limited improvement from controlling orientation implies that it was not possible for the users to overcome the positional difficulty of the task.

The 6-DOF frictional constraints without frictional redirection (FC6) were included within the experiments to identify if, and how, the frictional redirection assisted the user. The results show that the average performance for FC6 was significantly lower than DFC6 and lower than DFC3T. These results conform to the hypothesis behind frictional redirection that, once a user penetrates a constraint, a conventional frictional constraint will permit them to move parallel to the constraint indefinitely. It is expected that, if the speed of deformation on the pathway was increased, the difference between FC6 and those employing frictional redirection would become even more pronounced.

Full 6-DOF dynamic frictional constraints led to the best average user performance. It was significantly better than all methods in both metrics at the 95 % confidence interval, except DFC3T in contact percentage, for which it was at 90 %. The interesting aspect of this result is that DFC3R in isolation was of no significant benefit; however, combining it with DFC3T made a significant improvement. Hence, DFC6 was shown to be greater than the sum of its parts.

VI. CONCLUSIONS

A previous publication by the authors introduced the concept of a dynamic frictional constraint. This is a novel control formulation for robot assisted surgery, intended to assist a surgeon while operating within a dynamically changing environment. The core aspect of a dynamic frictional constraint is that it generates its assistance by redirecting and dissipating a surgeon's energy and never generates any energy of its own. This property prevents active forcing of the surgical tool by the robot, ensuring that the surgeon always maintains overall control.

In this paper the dynamic frictional constraint concept has been rederivied for translations in $\mathbb{R}^3$, proven to be dissipative and has been extended for rotations in SO(3). The energy redirection in the new formulation is based around the abstracted projection of a vector into a cone. The abstraction of this operation means that it can be applied to constrain both rotation and translation in an almost identical way.

To validate the effectiveness of the constraint formulation, a simulation of a dynamic task relying on accurate positioning and orientation was implemented. The experimental results showed that the method was of significant benefit when compared to cases without any assistance; with position and orientation constraints individually and where a conventional frictional constraint (without energy redirection) were used.

It was identified during these experiments, and stated previously in the literature [15], that due to their disconnect, often a user will not notice an error in either position or orientation if they are focussed on the other. It would therefore be likely that applying this concept of energy redirection between translation and rotation will improve the performance of dynamic frictional constraints even further. Implementing this coupling and integrating the method within a more clinical task will be the focus of future work.

APPENDIX

Simplification of the elasto-plastic friction model

When using the EP model to represent Coulomb friction, without elastic pre-sliding, the discrete operations in equations (12) and (13) of [8] reduce to a single saturation operation upon a candidate z value z_c which represents a fully elastic displacement.

Proof: By setting $f_{max} = f_C$ in the standard Coulomb model for EP friction (equation (6) in [8]), the steady-state z value $z_{ss}(\dot{x})$ (equation (9) in [8]) becomes:

$$z_{ss}(\dot{x}) = \begin{cases} z_{css} & \dot{x} \geq 0 \\ -z_{css} & otherwise \end{cases} \tag{22}$$

where $z_{css} = f_C/\sigma_0$.

This representation of $z_{ss}(\dot{x})$ allows the fractional inequality used in the EP model's saturation operations (equations (12) and (13)) to be represented as follows:

$$\frac{z}{z_{ss}(\dot{x})} < 1 \Leftrightarrow (|z| < z_{css}) \vee (\text{sgn}(\dot{x}) \neq \text{sgn}(z)) \tag{23}$$

Using this notation, a bi-directional step function, equivalent to that shown in figure 5 of [8] without the breakaway deflection, can be used to define $\alpha(z, \dot{x})$:

$$\alpha(z, \dot{x}) = \begin{cases} 0 & (|z| < z_{css}) \vee (\text{sgn}(\dot{x}) \neq \text{sgn}(z)) \\ 1 & otherwise \end{cases} \tag{24}$$

By the equivalence in equation (23), when the expression for $\alpha(z, \dot{x})$ in equation (24) is substituted into the top subfunction of equation (12) in [8] it is clear that $\forall z \forall \dot{x}\ \alpha(z, \dot{x}) = 0$. The function subsequently simplifies to:

$$y_k = \begin{cases} \Delta x_k & \frac{z_{k-1}}{z_{ss}(v_k)} < 1 \\ 0 & otherwise \end{cases} \tag{25}$$

From equation (25) it is known that:

$$\frac{z_{k-1}}{z_{ss}(v_k)} \geq 1 \implies y_k = 0 \tag{26}$$

Therefore it must also hold that:

$$\frac{z_{k-1}}{z_{ss}(v_k)} \geq 1 \implies \left(\frac{z_{k-1}}{z_{ss}(v_k)}\right) = \left(\frac{z_{k-1} + y_k}{z_{ss}(v_k)}\right) \tag{27}$$

Consolidation of the two saturation operations gives:

$$z_k = \begin{cases} z_c & \left(\frac{z_{k-1}}{z_{ss}(v_k)} < 1\right) \wedge \left(\frac{z_c}{z_{ss}(v_k)} < 1\right) \\ z_{ss}(v_k) & otherwise \end{cases} \tag{28}$$

where $z_c = z_{k-1} + \Delta x_k$ is the candidate z value representing a fully elastic displacement.

By expressing the conditions in equation (28) using the alternate form in equation (23), it can be seen that the first clause of the top subfunction is redundant and therefore this operation further simplifies to:

$$z_k = \begin{cases} z_c & (|z_c| < z_{css}) \vee (\text{sgn}(\dot{x}) \neq \text{sgn}(z_c)) \\ z_{ss}(v_k) & otherwise \end{cases} \tag{29}$$

As the magnitude of z_{css} is constant, it can be proven by induction that:

$$|z_c| \geq z_{css} \implies \text{sgn}(\dot{x}) = \text{sgn}(z_c) \tag{30}$$

Such that equation (29) reduces to:

$$z_k = \begin{cases} z_c & |z_c| < z_{css} \\ z_{ss}(v_k) & otherwise \end{cases} \tag{31}$$

Substituting the definition for $z_{ss}(v_k)$ from equation (22), and using the implication in equation (30), the final simplified equation for z_k is:

$$z_k = \begin{cases} z_c & |z_c| < z_{css} \\ z_{css} & z_c \geq z_{css} \\ -z_{css} & z_c \leq -z_{css} \end{cases} \tag{32}$$

■

Dissipativity of dynamic frictional constraints in $\mathbb{R}^3$

In general, a system is said to be dissipative [16] if $\forall t_1 \geq 0$ and $\forall t_2 \geq t_1$:

$$\int_{t_1}^{t_2} s\left(u(t), y(t)\right)\, dt \geq V(a(t_2)) - V(a(t_1)) \tag{33}$$

where $u(t)$ and $y(t)$ are the system inputs and outputs at time t respectively, $s(\cdot)$ is the supply rate of energy into the

system, $V(\cdot)$ is a continuous, non-negative storage function and $a(t)$ is the system state variable. Dynamic frictional constraints conform to this definition of dissipativity.

Proof: Dissipativity can be proven by substituting the robot power for the supply rate, the spring energy for the storage function and the elastic displacement for the system state variable in equation (33). The inequality subsequently becomes:

$$\int_{t_1}^{t_2} \mathbf{f}(t) \cdot \dot{\mathbf{x}}(t)\, dt \geq \frac{1}{2}\sigma_0 \|\mathbf{z}(t_2)\|^2 - \frac{1}{2}\sigma_0 \|\mathbf{z}(t_1)\|^2 \quad (34)$$

It is possible to prove this inequality by showing that $\forall t \geq 0$ the derivative of the storage function is never greater than the supply rate:

$$\mathbf{f}(t) \cdot \dot{\mathbf{x}}(t) \geq \frac{d}{dt}\frac{1}{2}\sigma_0 \|\mathbf{z}(t)\|^2 \quad (35)$$

$$\mathbf{f}(t) \cdot \dot{\mathbf{x}}(t) \geq \sigma_0 \|\mathbf{z}(t)\| \frac{d\|\mathbf{z}(t)\|}{dt} \quad (36)$$

Assuming that the damping elements of the constraint force are dissipative:

$$\sigma_0 \mathbf{z}(t) \cdot \dot{\mathbf{x}}(t) \geq \sigma_0 \|\mathbf{z}(t)\| \frac{d\|\mathbf{z}(t)\|}{dt} \quad (37)$$

$$\hat{\mathbf{z}}(t) \cdot \dot{\mathbf{x}}(t) \geq \frac{d\|\mathbf{z}(t)\|}{dt} \quad (38)$$

where the overhat symbol identifies a normalised vector.

Discretising the model at time k and dividing through by the time-step (making the assumption that the time-step is small such that $\dot{\mathbf{x}}_k \approx \dot{\mathbf{x}}_{k-1}$):

$$\hat{\mathbf{z}}_k \cdot \Delta\mathbf{x}_k \geq \|\mathbf{z}_k\| - \|\mathbf{z}_{k-1}\| \quad (39)$$

Equation (39) is initially proven for the first and second subfunctions of equation (15) by substituting in:

$$\Delta\mathbf{x}_k = \beta\mathbf{z}_k - \mathbf{z}_{k-1} \quad \text{where} \quad \beta \geq 1 \quad (40)$$

Giving:

$$\hat{\mathbf{z}}_k \cdot (\beta\mathbf{z}_k - \mathbf{z}_{k-1}) \geq \|\mathbf{z}_k\| - \|\mathbf{z}_{k-1}\| \quad (41)$$

$$\beta\|\mathbf{z}_k\| - \|\mathbf{z}_k\| + \|\mathbf{z}_{k-1}\| \geq \hat{\mathbf{z}}_k \cdot \mathbf{z}_{k-1} \quad (42)$$

Applying Cauchy's inequality to the right hand side:

$$\beta\|\mathbf{z}_k\| - \|\mathbf{z}_k\| + \|\mathbf{z}_{k-1}\| \geq \|\mathbf{z}_{k-1}\| \quad (43)$$

$$\beta \geq 1 \quad (44)$$

■

Equation (39) is next proven for the third subfunction of equation (15) when $\hat{\mathbf{y}} \cdot \mathbf{z}_c \leq 0$. Considering equation (16):

$$\hat{\mathbf{y}} \cdot \mathbf{z}_c \leq 0 \implies \|\mathbf{z}_k\| = 0 \quad (45)$$

By substituting $\|\mathbf{z}_k\| = 0$ into equation (37), both left and right hand sides become zero proving the inequality. ■

Equation (39) is finally proven for the third subfunction of equation (15), when $\hat{\mathbf{y}} \cdot \mathbf{z}_c > 0$, by substituting in:

$$\mathbf{z}_k = \gamma\left(\hat{\mathbf{y}} \cdot \mathbf{z}_c\right)\hat{\mathbf{y}} \quad \text{where} \quad 1 \geq \gamma \geq 0 \quad (46)$$

$$\Delta\mathbf{x}_k = \mathbf{z}_c - \mathbf{z}_{k-1} \quad (47)$$

and considering equation (16) such that:

$$\hat{\mathbf{y}} \cdot \mathbf{z}_c > 0 \implies \|\mathbf{z}_k\| > 0 \implies \hat{\mathbf{z}}_k = \hat{\mathbf{y}} \quad (48)$$

Giving:

$$\hat{\mathbf{y}} \cdot (\mathbf{z}_c - \mathbf{z}_{k-1}) \geq \gamma\left(\hat{\mathbf{y}} \cdot \mathbf{z}_c\right) - \|\mathbf{z}_{k-1}\| \quad (49)$$

$$\hat{\mathbf{y}} \cdot \mathbf{z}_c - \gamma\left(\hat{\mathbf{y}} \cdot \mathbf{z}_c\right) + \|\mathbf{z}_{k-1}\| \geq \hat{\mathbf{y}} \cdot \mathbf{z}_{k-1} \quad (50)$$

Applying Cauchy's inequality to the right hand side:

$$\hat{\mathbf{y}} \cdot \mathbf{z}_c - \gamma\left(\hat{\mathbf{y}} \cdot \mathbf{z}_c\right) + \|\mathbf{z}_{k-1}\| \geq \|\mathbf{z}_{k-1}\| \quad (51)$$

$$1 \geq \gamma \quad (52)$$

■

ACKNOWLEDGMENT

This work was supported by EU Grant FP7-ICT-2009-6-270460. The authors thank Dr Fernando Bello and the Simulation and Modelling in Medicine and Surgery (SiMMS) research group at Imperial College London for the use of their research facilities.

REFERENCES

[1] B. Davies, M. Jakopec, S. J. Harris, F. Rodriguez y Baena, A. Barrett, A. Evangelidis, P. Gomes, J. Henckel, and J. Cobb, "Active-constraint robotics for surgery," *Proc. IEEE*, vol. 94, no. 9, pp. 1696–1704, 2006.

[2] L. B. Rosenberg, "Virtual fixtures: Perceptual tools for telerobotic manipulation," in *Proc. IEEE Virt. Real. Annual Int. Symp.*, sept. 1993, pp. 76 –82.

[3] S. A. Bowyer, B. L. Davies, and F. Rodriguez y Baena, "Active constraints/virtual fixtures: A survey," *IEEE Trans. Robot.*, vol. 30, no. 1, pp. 138–157, feb. 2014.

[4] K.-W. Kwok, K. H. Tsoi, V. Vitiello, J. Clark, G. Chow, W. Luk, and G.-Z. Yang, "Dimensionality reduction in controlling articulated snake robot for endoscopy under dynamic active constraints," *IEEE Trans. Robot.*, vol. 29, no. 1, pp. 15–31, 2013.

[5] J. G. Petersen and F. Rodriguez y Baena, "A dynamic active constraints approach for hands-on robotic surgery," in *Proc. IEEE/RSJ Int. Conf. Intell. Robot. Syst.*, 2013, pp. 1966–1971.

[6] S. A. Bowyer and F. Rodriguez y Baena, "Dynamic frictional constraints for robot assisted surgery," in *Proc. IEEE World Haptics Conf.*, 2013, pp. 319–324.

[7] R. Kikuuwe, N. Takesue, and H. Fujimoto, "A control framework to generate nonenergy-storing virtual fixtures: Use of simulated plasticity," *IEEE Trans. Robot.*, vol. 24, no. 4, pp. 781–793, aug. 2008.

[8] V. Hayward, B. S. R. Armstrong, F. Altpeter, and P. E. Dupont, "Discrete-time elasto-plastic friction estimation," *IEEE Trans. Control Syst. Technol.*, vol. 17, no. 3, pp. 688 –696, may 2009.

[9] C. Canudas de Wit, H. Olsson, K. Astrom, and P. Lischinsky, "A new model for control of systems with friction," *IEEE Trans. Autom. Control*, vol. 40, no. 3, pp. 419–425, mar. 1995.

[10] B. Brogliato, R. Lozano, B. Maschke, and O. Egeland, *Dissipative Systems Analysis and Control: Theory and Applications*. Springer-Verlag, 2007.

[11] E. B. Dam, M. Koch, and M. Lillholm, "Quaternions, interpolation and animation," Department of Computer Science, University of Copenhagen, Tech. Rep. DIKU-TR-98/5, 1998.

[12] F. Pearson, *Map Projections: Theory and Applications*. CRC Press Inc., 1990.

[13] R. I. Hartley and F. Kahl, "Global optimization through rotation space search," *Int J. Comput Vis.*, vol. 82, pp. 64–79, 2009.

[14] R. G. D. Steel, J. H. Torrie, and D. A. Dickey, *Principles and Procedures of Statistics: A Biometrical Approach*, 3rd ed. McGraw-Hill, Inc., 1997.

[15] R. Castillo-Cruces and J. Wahrburg, "Virtual fixtures for autonomous error compensation for human-robot cooperative tasks," *Robotica*, vol. 28, pp. 267–277, 2010.

[16] J. C. Willems, "Dissipative dynamical systems," *Euro. J. Control*, vol. 13, pp. 134–151, 2007.